

Ultra-uniform Nanocrystalline Materials via Two-Step Sintering

Yanhao Dong¹ (dongyh@mit.edu), Hongbing Yang², Dong Ding³, Ju Li^{1,4},

Jiangong Li², I-Wei Chen⁵

¹Department of Nuclear Science and Engineering, Massachusetts Institute of Technology, Cambridge, MA 02139, USA

²Institute of Materials Science and Engineering and MOE Key Laboratory for Special Functional Materials and Structure Design, Lanzhou University, Lanzhou 730000, China

³Energy & Environmental Science and Technology, Idaho National Laboratory, Idaho Falls, ID 83415, USA

⁴Department of Materials Science and Engineering, Massachusetts Institute of Technology, Cambridge, MA 02139, USA

⁵Department of Materials Science and Engineering, University of Pennsylvania, Philadelphia, PA 19104, USA

Keywords: Nanocrystalline materials, microstructure, grain growth, sintering, alumina

Nanocrystalline metals and ceramics with <100 nm grain sizes and superior properties are of great interest. Much has been discussed about achieving nano grains, but little is known about maintaining grain-size uniformity that is critical for material reliability. An especially intriguing question is whether it is possible

to achieve a size distribution narrower than the one theoretically predicted by Hillert¹ for normal grain growth, a possibility suggested—for growth with a higher growth exponent—by the generalized growth theory² unifying the mean-field models of Lifshitz, Slyozov, Wagner (LSW)^{3,4} and Hillert. We show that this can be realized in an appropriately designed two-step sintering route that (a) takes advantage of the large growth exponent in the intermediate sintering stage to form an ultra-uniform porous microstructure, and (b) freezes the grain growth thereon while continuing densification to reach a full density. The resultant dense Al₂O₃ ceramic has an average grain size of 34 nm and a much narrower size distribution than predicted by Hillert.

Rapid development of nanocrystalline materials in the past decades has provided much room for improved and emerging properties at the bottom.⁵⁻⁷ While the benefits of nano-structuring (e.g., grain boundary strengthening via the Hall-Petch relationship) is usually attributed to the average grain size, it is the size distribution that matters most to engineering reliability.^{8,9} This is because mechanical, electrical, dielectric, and other failures dictated by an instantaneous or a gradual breakdown event typically happen at the weakest point, which in a polycrystalline material is often associated with a microstructural or chemical inhomogeneity at some grain/grain boundary of an extreme size. Reducing grain size dispersion in nanocrystalline materials is thus a critical challenge.

For polycrystals that follow normal grain growth, in which grain boundaries

presumably all have the same energy and mobility and they move to lower the grain boundary energy, Hillert made a theoretical prediction that the standard deviation of the grain size distribution relative to the average grain size, to be denoted as σ , should be 35.4%.¹ Real materials do not have the same energy and mobility for all grain boundaries, which explains why experimental studies always found a much broader size distribution than Hillert's prediction. This is shown by the blue data points in **Fig. 1** for a large number of ceramics sintered in various conventional ways^{8,10-45}, all having a relative standard deviation σ larger than Hillert's prediction. Indeed, a combination of a small σ and a small average grain size G_{avg} provides a measure of material "quality," and the tendency that they increase together as in **Fig. 1** may in part explain the appeal of nano materials. This seems to suggest that Hillert's 35.4% standard deviation may be regarded as a lower limit of grain size uniformity, and it may be difficult if not impossible to do better in real materials, including nanomaterials. Whether this proposition can be challenged or not is of much interest in view of the engineering importance of grain size uniformity mentioned above.

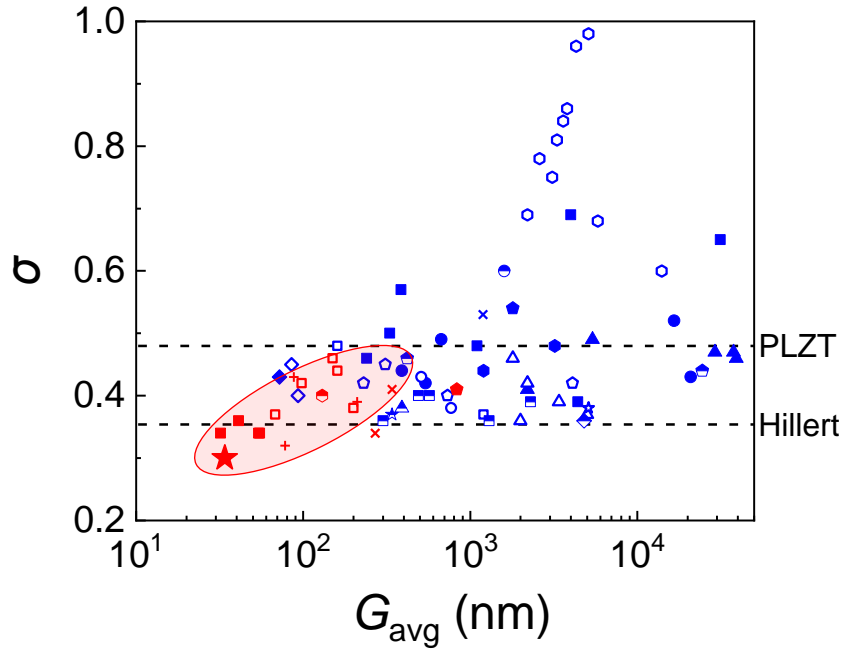


Figure 1 “Quality plot” in G_{avg} and σ of sintered materials. Comparison of G_{avg} and σ of 22 dense materials (represented by 22 different types of symbols), variously sintered as reported in literature and this work (star at lower-left corner). Two-step sintered in red, conventionally sintered in blue; data, type-labeling, and references listed in **Supplementary Table S1**. Lower dashed line: Hillert’s theoretical prediction.¹ Upper dashed line: hot-pressed transparent (Pb,La)(Zr,Ti)O₃ (PLZT) with a known uniform microstructure.³³ Shadowed ellipse is for guidance of eyes.

Outside the field of bulk nanocrystalline materials, it is well known that essentially mono-sized nanoparticles can be obtained by liquid-phase precipitation, growth and coarsening—also called Ostwald ripening, and Ostwald ripening is described by the same LSW model.^{3,4,46,47} The common rationale for such uniformity is: in LSW coarsening, not only the driving force diminishes with size because of the

familiar size dependence of capillary pressure, but also the diffusion distance increases with size, thus causing the overall growth rate to rapidly decay as the particle coarsens. Mathematically, this observation of faster approach to growth/coarsening stagnation is reflected in a higher growth exponent n , defined by (particle/grain size) ^{n} \sim time, which is 3 in Oswald ripening and 2 in normal grain growth. Therefore, one stands to reason that the size distribution narrows with the growth exponent, and if a higher growth exponent can be somehow engineered in sintering, it would be possible to obtain a more uniform microstructure than predicted by Hillert. If so, then ultimate nanomaterials in the lower left corner of **Fig. 1** with an ultra-fine as well as ultra-uniform grain size can be realized. How to achieve this in theory and in practice to produce a number of such materials including a dense Al₂O₃ with 34 nm grain size and $\sigma=0.30$, as indicated by the red star in **Fig. 1**, is the subject of this work.

The above reasoning is supported by the analytic solution of steady-state size distribution of the growth equation², initially formulated by LSW^{3,4} and Hillert¹,

$$\frac{dG}{dt} = 2M\gamma \left(\frac{G}{a}\right)^{\alpha} \left(\frac{1}{G_{cr}} - \frac{1}{G}\right) \quad (1)$$

Here, α is 0 in normal grain growth and -1 in LSW (Ostwald ripening), G is the size of a growing or shrinking grain/particle, $2\gamma/G$ with γ being the interfacial energy is the capillary pressure, G_{cr} is the critical grain/particle size that neither grows nor shrinks at time t —thereby determining a chemical potential $2\gamma/G_{cr}$ for the system that ensures mass/volume conservation at the same time t , M is the grain boundary mobility in

grain growth or $M = \frac{D}{k_B T} \frac{\Omega}{a}$ (with D the diffusivity, Ω the atomic volume and $k_B T$

has their usual meaning) in particle growth, and a is a length (e.g., atomic spacing) that preserves the dimension. For an arbitrary $\alpha \leq 1$, a power-law $G_{\text{avg}}^n \sim t$ obtains with a growth exponent $n=2-\alpha \geq 1$, and there is a close form solution² of the steady-state size distribution $P'(u)$ with normalized size $u=G/G_{\text{cr}}$

$$P'(u) = \frac{3u^{1-\alpha}}{u^{2-\alpha} - \frac{(2-\alpha)^{2-\alpha}}{(1-\alpha)^{1-\alpha}}(u-1)} \exp \left[-\frac{3}{2-\alpha} \int_0^u \frac{-(2-\alpha)u^{1-\alpha}}{\frac{(2-\alpha)^{2-\alpha}}{(1-\alpha)^{1-\alpha}}(u-1) - u^{2-\alpha}} du \right] \quad (2)$$

A more convenient distribution is obtained by using the normalized grain size G/G_{avg} obtained from $u = \frac{G}{G_{\text{avg}}} u_{\text{avg}}$, where $u_{\text{avg}} = \int_0^{u_0} u P'(u) du$. The corresponding size distribution $P(G/G_{\text{avg}})$ is shown in **Fig. 2**, which clearly illustrates that $P(G/G_{\text{avg}})$ sharpens as α decreases and n increases; meanwhile, its standard deviation σ ($\sigma = \Sigma/G_{\text{avg}}$, where Σ is the standard deviation of grain size) decreases as shown in the inset of **Fig. 2**.

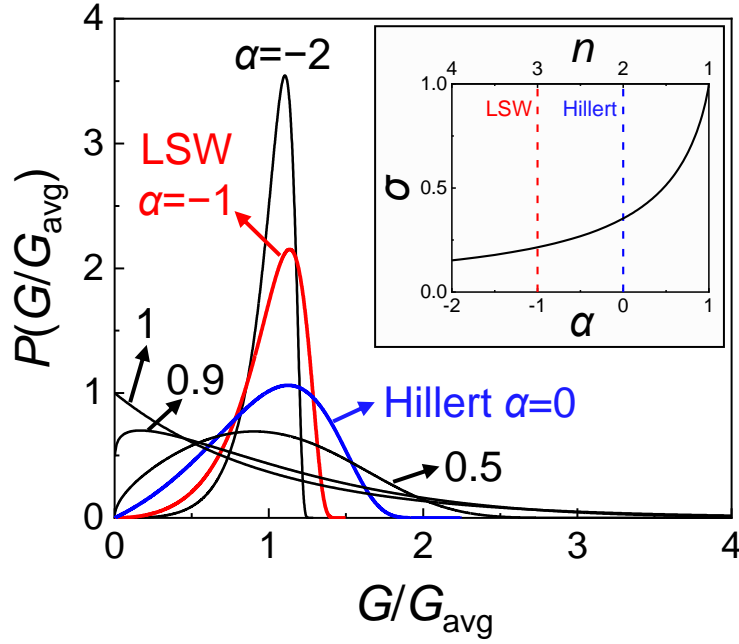


Figure 2 Steady-state solution of generalized growth equation. Calculated normalized grain size distribution $P(G/G_{\text{avg}})$ as a function of α . Inset: Calculated standard deviations σ for G/G_{avg} as a function of α and n .

Normal grain growth with $n=2$ was firmly established in dense ceramics, e.g., undoped or variously doped Y_2O_3 , CeO_2 and ZrO_2 .^{20,21,38} Furthermore, it is well known that grain growth in pore-containing ceramics follows $n \geq 3$ because the grain boundaries of a larger grain are statistically in contact with more pores, hence sense stronger pinning force.⁴⁸ The latter also applies to intermediate-stage sintering, defined as sintering of a powder compact in which particles are already sinter-bonded but still separated by mostly open porosity (namely interconnected pore channels) and not isolated pores (as in the final stage sintering). If so, the relative standard deviation of the grain/particle size distribution of this state should be smaller than that predicted

by Hillert, and it could offer a “template” to grow ultra-uniform nanomaterials.

To examine this possibility, we pressurelessly sintered high-purity Al_2O_3 powder compacts to intermediate densities by heating them to various temperatures, then cooling them down without holding at the highest temperature. (See **Methods** for experimental details.) As shown in **Fig. 3a**, both the average grain size G_{avg} (open circles) and its standard deviation Σ (plotted as error bar) measured from the transmission electron microscopy (TEM) images of fractured fragments monotonically decrease with increasing relative density ρ , but their ratio $\sigma = \Sigma/G_{\text{avg}}$ shown as open circles in **Fig. 3c** initially decreases, then reaches a minimum at $\rho=65\%$ before rising at higher density. The same trend was confirmed in **Fig. 3b** (G_{avg} as filled circles and Σ as error bars) and **Fig. 3c** (σ as filled circles) by the data measured from the images of scanning electron microscopy (SEM) of fractured and thermally etched surfaces of the same set of samples. Importantly, σ during much of the porous regime of 60-85% falls significantly below Hillert’s $\sigma=0.354$, shown in **Fig. 2c** as a dashed horizontal line.

The ultra-uniform microstructure of porous ceramics sintered to the intermediate stage is evident from the micrograph and grain size histogram of an Al_2O_3 sample of 84% with $\sigma = 0.31$, shown in **Fig. 4a-b**, taken from the SEM images of fractured and thermally etched surfaces. A comparably small σ (0.30) was also obtained in another ceramic, 8 mol% yttria stabilized zirconia (8YSZ), pressurelessly sintered to $\rho=69\%$, as shown by the orange square in **Fig. 3c**, measured from the SEM images of polished and thermally etched surfaces. Its micrograph and grain size histogram (**Fig. 4c-d**)

again portray a highly uniform microstructure despite the prominent presence of open pore channels.

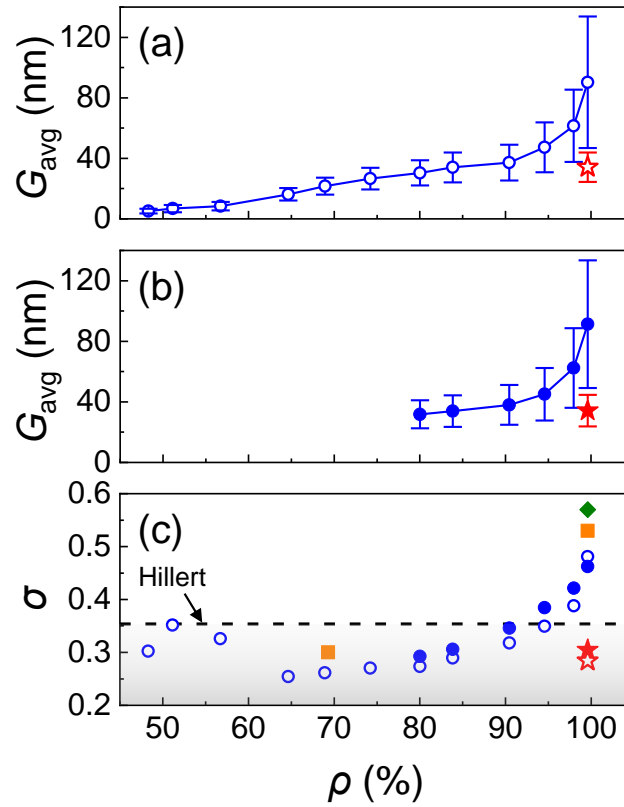


Figure 3 Microstructural dispersity in porous and dense polycrystals. Trajectory of G_{avg} (average grain size) vs. relative density ρ of Al_2O_3 ceramics measured under (a) TEM in open symbols and (b) SEM in closed symbols, with standard deviation Σ shown as error bars. Two-step sintering data at full density also plotted as stars. (c) Relative standard deviation, $\sigma = \Sigma / G_{\text{avg}}$, from (a-b) using same symbols. Also included are orange square at $\rho = 69\%$: 8YSZ heated to reach said density; orange square (8YSZ) and green diamond (Al_2O_3) at $\rho \approx 100\%$: samples annealed for additional time at highest temperature after reaching nearly full density. (See text for details.)

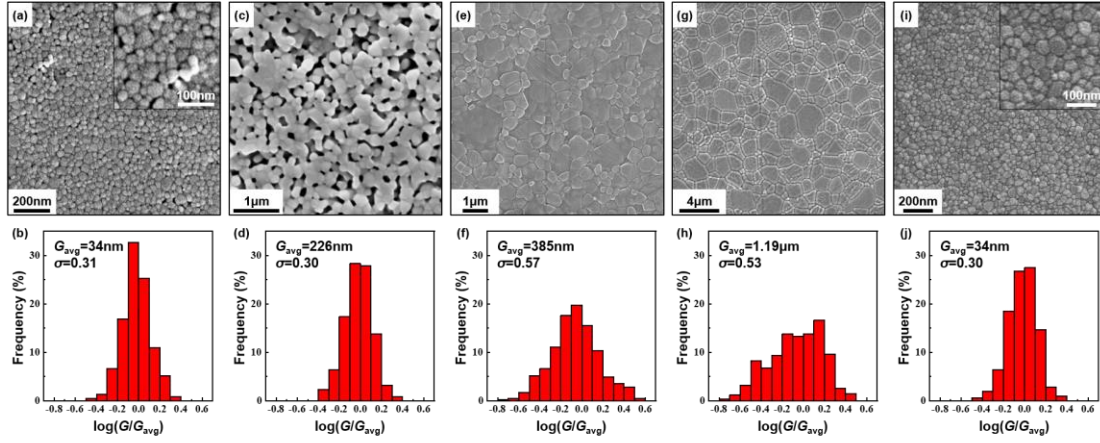


Figure 4 Comparison of microstructural uniformity. SEM micrographs and normalized grain size histograms of (a-b) Al_2O_3 heated to 1150°C without holding, $\rho=84\%$; inset in (a): enlarged section showing porosity; (c-d) 8YSZ heated to 1280°C without holding, $\rho=69\%$; (e-f) dense Al_2O_3 sintered at 1300°C for 10 h; (g-h) dense 8YSZ sintered at 1300°C for 12 h; and (i-j) dense two-step sintered Al_2O_3 reaching 1150°C (T_1) without holding and then held at 1025°C (T_2) for 40 h; inset in (i): enlarged section showing absence of porosity. Also listed in histograms are G_{avg} and σ .

Although a remarkably small σ throughout the intermediate stage of sintering is now established, unfortunately uniformity invariably deteriorates as the density exceeds 90% (see **Fig. 3c**), which marks the onset of final-stage sintering in most materials.^{49,50} To make matter worse, it is typical to hold the material at the highest sintering temperature for additional time period to assure full densification, but such practice causes concurrent grain growth that increases σ further. For example, σ reached 0.57 in an Al_2O_3 ceramic (measured from SEM) after 10 h annealing after

attaining nearly full density, as indicated by the green diamond at $\rho=100\%$ in **Fig. 3c**. It has a visibly deteriorated microstructure (**Fig. 4e**) and grain size histogram (**Fig. 4f**), making it much less uniform than the 84% dense sample in **Fig. 4a-b**. The same holds for 8YSZ after 12 h holding after attaining nearly full density: it features a much larger σ (0.53, orange square at $\rho=100\%$ in **Fig. 3c**) and a visibly less uniform microstructure (**Fig. 4g-h**) than its porous counterpart in **Fig. 4c-d**.

Clearly, one needs a very different strategy from conventional sintering to freeze the outstanding microstructure of intermediate-stage sintering so that it can be used as a template throughout final-stage sintering. In the past 20 years, two-step sintering⁵¹ has been shown to do exactly that: it effects densification without grain growth, thus freezing the microstructure while improving the density, and it has been successfully demonstrated in numerous oxides, nitrides, carbides and some metals.^{8,15-17,36,37,43-45,51-55} This process proceeds by first heating the powder compact to a higher temperature (designated as T_1), without holding, to reach a high enough density, then lowering the temperature to T_2 and holding there for an extended time to reach full density. To succeed, the post- T_1 density should be high enough to render all remaining pores/pore channels unstable, which occurs when their surface curvature changes from negative to positive (e.g., a spherical pore has a uniformly positive surface curvature of $2/\text{radius}$). For Al_2O_3 , which has a relatively large anisotropy in the surface energy and grain boundary energy, this density should be relatively high. So we used $T_1=1150^\circ\text{C}$ to reach $\rho=84\%$, then cooled the sample down to $T_2=1025^\circ\text{C}$ and held there for 40 h, to finally obtain a 99.6% dense ceramic (detailed sintering

kinetics reported in [Ref. 55](#)). With the microstructure in **Fig. 4i** and the grain size histogram in **Fig. 4j**, it has essentially the same G_{avg} (34 nm, also shown in **Fig. 3a-b** by stars, open ones from TEM and filled ones from SEM) and σ (0.30, also shown in **Fig. 3c** from the red error bars in **Fig. 3a-b**) as those of the 84% dense sample (the sample before cooling down to T_2 , **Fig. 3a-b**.) Therefore, having faithful templating achieved during T_2 sintering, we have demonstrated the feasibility of obtaining a dense nanocrystalline Al_2O_3 with ultra-uniformity, which is shown as a star in red in **Fig. 1**. As also shown in **Fig. 1**, two-step sintered nanograin Al_2O_3 ceramics of a lightly higher σ were too obtained in two of our recent studies.^{15,16} Other two-step sintered ceramics and metals reported in the literature also tend to cluster near the lower left corner of **Fig. 1** (in red), although they all have larger G_{avg} and higher σ , presumably because of less than optimal powder processing and sintering schedule, and/or inadequate suppression of grain growth during T_2 sintering.

It has been recently established that while densification at T_2 proceeds by grain boundary diffusion, the low mobility of three-grain or four-grain junctions at such temperature can suppress grain growth.^{45,51} However, after a very long time, a new grain size distribution can still develop, which will feature a broader size distribution because the grain growth exponent tends to be smaller for grain growth that is rate-limited by three-grain and four-grain junctions (e.g., $n=1$ under three-grain-junction control assuming the number of such junctions is size-independent).⁴⁵ Therefore, to assure the success of two-step sintering, the time spent at T_2 must be judiciously selected: long enough to obtain full densification, but

not too long to trigger eventual grain growth. Provided such best practice is followed, no perceptible grain growth should occur and the ultra-uniform microstructure of intermediate-stage sintering can be preserved while density improves, as we have found here and elsewhere for Al_2O_3 .^{15,16,55} Hopefully, the above new theoretical insight and success in obtaining a dense nanocrystalline Al_2O_3 with ultra-uniformity much exceeding the theoretical “limit” predicted by Hillert 60 years ago will encourage the development of other ultra-uniform nanocrystalline materials with superior properties and reliability.

Methods

Powders of $\alpha\text{-Al}_2\text{O}_3$ (purity: 99.958%, average particle size: 4.7 nm) were prepared by high-energy ball milling followed by corrosion and separation.⁵⁶ Pressed pellets of powders were heated in air at 10°C/min to various temperatures, then either held there for a certain holding time or immediately cooled as specified in **Supplementary Information**. Two-step sintering was conducted by firstly heating the pellet at 10°C/min to 1150°C, then, without holding, immediately cooling it to 1025°C and held at that temperature for 40 h. Fractured fragments of sintered pellets were examined under a transmission electron microscope (TEM; FEI Tecnai G2 F30). Likewise, fractured and thermally etched (at 50 °C lower than sintering temperature for 0.5 h) surfaces of the pellets were examined under a scanning electron microscope (SEM; Tescan LYRA3 XMU). Pressed pellets of 8YSZ powders (TZ-8Y, Tosoh Co., Tokyo, Japan) were similarly heated in air to 1280°C without holding, or to 1300°C

and held there for 12 h, both using 5°C/min during heating. Polished and thermally etched (1220°C for 0.2 h) surfaces of 8YSZ were examined under SEM (Quanta 600, FEI Co.). Average grain sizes and grain size distributions were calculated by measuring the sizes along a random direction of N grains ($N=300-600$). For more details, see **Supplementary Information**.

References

1. Hillert, M. On the theory of normal and abnormal grain growth. *Acta Mater.* **13**, 227-238 (1965).
2. Dong, Y., Chen, I. W. Grain growth with size-dependent or statistically distributed mobility. Preprint at <https://arxiv.org/abs/1708.04092> (2017).
3. Lifshitz, I. M., Slyozov, V. V. The kinetics of precipitation from supersaturated solid solutions. *J. Phys. Chem. Solids* **19**, 35-50 (1961).
4. Wagner, C. Z. Theorie der alterung von niederschlägen durch umlösen (ostwald-reifung). *Berichte der Bunsengesellschaft für physikalische Chemie* **65**, 581-591 (1961).
5. Chookajorn, T., Murdoch, H. A., Schuh, C. A. Design of stable nanocrystalline alloys. *Nature* **337**, 951-954 (2012).
6. Amram, D., Schuh, C.A. Higher temperatures yield smaller grains in a thermally stable phase-transforming nanocrystalline alloy. *Phys. Rev. Lett.* **121**, 145503 (2018).
7. Zhou, X., Li, X. Y., Lu, K. Enhanced thermal stability of nanograined metals below a critical grain size. *Science* **360**, 526-530 (2018).

8. Zhao, Q., Gong, H., Wang, X., Chen, I. W., Li, L. Superior reliability via two-step sintering: Barium titanate ceramics. *J. Am. Ceram. Soc.* **99**, 191-197 (2016).
9. Evans, A. G. Structural reliability: A processing-dependent phenomenon. *J. Am. Ceram. Soc.* **65**, 127-137 (1982).
10. Xue, L. A., Chen, I. W. Deformation and grain growth of low-temperature-sintered high-purity alumina. *J. Am. Ceram. Soc.* **73**, 3518-3521 (1990).
11. Dillon, S. J., Harmer, M. P. Relating grain-boundary complexion to grain-boundary kinetics I: Calcia-doped alumina. *J. Am. Ceram. Soc.* **91**, 2304-2313 (2008).
12. Dillon, S. J., Harmer, M. P. Relating grain boundary complexion to grain boundary kinetics II: Silica-doped alumina. *J. Am. Ceram. Soc.* **91**, 2314-2320 (2008).
13. Kim, B.-N., Hiraga, K., Morita, K., Yoshida, H. Spark plasma sintering of transparent alumina. *Scripta Mater.* **57**, 607-610 (2007).
14. Lin, F. J. T., De Jonghe, L. C., Rahaman, M. N. Microstructure refinement of sintered alumina by a two-step sintering technique. *J. Am. Ceram. Soc.* **80**, 2269-2277 (1997).
15. Guo, R., Cao, W., Mao, X., Li, J. Selective corrosion preparation and sintering of disperse α -Al₂O₃ nanoparticles. *J. Am. Ceram. Soc.* **99**, 3556-3560 (2016).
16. Cao, W., Mao, X., Yuan, Y., Li, L., Zhao, L., Li, J. Sintering kinetics of disperse ultrafine equiaxed α -Al₂O₃ nanoparticles. *J. Eur. Ceram. Soc.* **37**, 4005-4013 (2017).
17. Wang, X., Deng, X., Bai, H., Zhou, H., Qu, W., Li, L., Chen, I. W. Two-step

- sintering of ceramics with constant grain-size, II: BaTiO₃ and Ni-Cu-Zn ferrite. *J. Am. Ceram. Soc.* **89**, 438-443 (2006).
18. Wang, S., Zhang, L., Zhang, L., Brinkman, K., Chen, F. Two-step sintering of ultrafine-grained barium cerate proton conducting ceramics. *Electrochem. Acta* **87**, 194-200 (2013).
 19. Zhou, X., Liu, L., Zhen, J., Zhu, S., Li, B., Sun, K., Wang, P. Ionic conductivity, sintering and thermal expansion behaviors of mixed ion conductor BaZr_{0.1}Ce_{0.7}Y_{0.1}Yb_{0.1}O_{3-δ} prepared by ethylene diamine tetraacetic acid assisted glycine nitrate process. *J. Power Sources* **196**, 5000-5006 (2011).
 20. Chen, P. L., Chen, I. W. Grain growth in CeO₂: Dopant effects, defect mechanism, and solute drag. *J. Am. Ceram. Soc.* **79**, 1793-1780 (1996).
 21. Dong, Y., Wang, H., Chen, I. W. Electrical and hydrogen reduction enhances kinetics in doped zirconia and ceria: I. Grain growth study. *J. Am. Ceram. Soc.* **100**, 876-886 (2017).
 22. Esposito, V., Ni, D. W., He, Z., Zhang, W., Prasad, A. S., Glasscock, J. A., Chatzichristodoulou, C., Ramousse, S., Kaiser, A. Enhanced mass diffusion phenomena in highly defective doped ceria. *Acta Mater.* **61**, 6290-6300 (2013).
 23. Rubio-Marcos, F., Ochoa, P., Fernandez, J. F. Sintering and properties of lead-free (K,Na,Li)(Nb,Ta,Sb)O₃ ceramics. *J. Eur. Ceram. Soc.* **27**, 4125-4129 (2007).
 24. Tsai, C.-L., Roddatis, V., Chandran, C. V., Ma, Q., Uhlenbruck, S., Bram, M., Heitjans, P., Guillon, O. Li₇La₃Zr₂O₁₂ interface modification for Li dendrite prevention. *ACS Appl. Mater. Interfaces* **8**, 10617-10626 (2016).

25. Sharafi, A., Haslam, C. G., Kerns, R. D., Wolfenstine, J., Sakamoto, J. Controlling and correlating the effect of grain size with the mechanical and electrochemical properties of $\text{Li}_7\text{La}_3\text{Zr}_2\text{O}_{12}$ solid-state electrolyte. *J. Mater. Chem. A* **5**, 21491-21504 (2017).
26. Marrero-Lopez, D., Ruiz-Morales, J. C., Pena-Martinez, J., Martin-Sedeno, M. C., Ramos-Barrado, J. R. Influence of phase segregation on the bulk and grain boundary conductivity of LSGM electrolytes. *Solid State Ionics* **186**, 44-52 (2011).
27. Yu, S., Bi, H., Sun, J., Zhu, L., Yu, H., Lu, C., Liu, X. Effect of grain size on the electrical properties of strontium and magnesium doped lanthanum gallate electrolytes. *J. Alloy Compd.* **777**, 244-251 (2019).
28. Rambabu, B., Ghosh, S., Zhao, W., Jena, H. Innovative processing of dense LSGM electrolytes for IT-SOFC's. *J. Power Sources* **159**, 21-28 (2006).
29. An, L., Ito, A., Goto, T. Effect of sintering temperature on the transparency and mechanical properties of lutetium aluminum garnet fabricated by spark plasma sintering. *J. Eur. Ceram. Soc.* **32**, 3097-3102 (2012).
30. Ehre, D., Chaim, R. Abnormal Hall-Petch behavior in nanocrystalline MgO ceramics. *J. Mater. Sci.* **43**, 6139-6143 (2008).
31. Sokol, M., Halabi, M., Kalabukhov, S., Frage, N. Nano-structured MgAl_2O_4 spinel consolidated by high pressure spark plasma sintering (HPSPS). *J. Eur. Ceram. Soc.* **37**, 755-762 (2017).
32. Shimizu, H., Kobayashi, K., Mizuno, Y., Randall, C. A. Advantages of low partial pressure of oxygen processing of alkali niobate: NaNbO_3 . *J. Am. Ceram. Soc.* **97**,

1791-1796 (2014).

33. Haertling, G. H. Piezoelectric and electrooptic ceramics. In *Ceramic Materials for Electronics* (ed. Buchanan, R. C.) 139-225 (Marcel Dekker, New York, 1991).

34. Yoshikawa, Y., Tsuzuki, K. Fabrication of transparent lead lanthanum zirconate titanate ceramics from fine powders by two-stage sintering. *J. Am. Ceram. Soc.* **75**, 2520-2528 (1992).

35. Rheinheimer, W., Hoffmann, M. J. Grain growth transitions of perovskite ceramics and their relationship to abnormal grain growth and bimodal microstructures. *J. Mater. Sci.* **51**, 1756-1765 (2016).

36. Mazaheri, M., Razavi Hesabi, Z., Sadrnezhad, S. K. Two-step sintering of titania nanoceramics assisted by anatase-to-rutile phase transformation. *Scripta Mater.* **59**, 139-142 (2008).

37. Li, X., Zhang, L., Dong, Y., Gao, R., Qin, M., Qu, X., Li, J. Pressureless two-step sintering of ultrafine-grained tungsten. *Acta Mater.* **186**, 116-123 (2020).

38. Chen, P. L., Chen, I. W. Grain boundary mobility in Y_2O_3 : Defect mechanism and dopant effects. *J. Am. Ceram. Soc.* **79**, 1801-1809 (1996).

39. Chaim, R., Kalina, M., Shen, J. Z. Transparent yttrium aluminum garnet (YAG) ceramics by spark plasma sintering. *J. Eur. Ceram. Soc.* **27**, 3331-3337 (2007).

40. Ikesue, A. Polycrystalline Nd:YAG ceramics lasers. *Opt. Mater.* **19**, 183-187 (2002).

41. Paladino, A. E., Maguire, E. A. Microstructure development in yttrium iron garnet. *J. Am. Ceram. Soc.* **53**, 98-102 (1970).

42. Savary, E., Marinel, S., Colder, H., Harnois, C., Lefevre, F. X., Retoux, R. Microwave sintering of nano-sized ZnO synthesized by a liquid route. *Powder Tech.* **208**, 521-525 (2011).
43. Mazaheri, M., Simchi, A., Golestani-Fard, F. Densification and grain growth of nanocrystalline 3Y-TZP during two-step sintering. *J. Eur. Ceram. Soc.* **28**, 2933-2939 (2008).
44. Mazaheri, M., Valefi, M., Razavi Hesabi, Z., Sadrnezhad, S. K. Two-step sintering of nanocrystalline 8Y₂O₃ stabilized ZrO₂ synthesized by glycine nitrate process. *Ceram. Int.* **35**, 13-20 (2009).
45. Dong, Y., Chen, I.W. Mobility transition at grain boundaries in two-step sintered 8 mol% yttria-stabilized zirconia. *J. Am. Ceram. Soc.* **101**, 1857-1869 (2018).
46. Murray, C. B., Norris, D. J., Bawendi, M.G. Synthesis and characterization of nearly monodisperse CdE (E = S, Se, Te) semiconductor nanocrystallites. *J. Am. Chem. Soc.* **115**, 8706-8715 (1993).
47. Voorhees, P. W. The theory of Ostwald ripening. *J. Stat. Phys.* **38**, 231-252 (1985).
48. Kingery, W. D., Bowen, H. K., Uhlmann, D. R. In *Introduction to Ceramics*, second edition, 454-455 (John Wiley & Sons, 1976).
49. Hassold, G. N., Chen, I. W., Srolovitz, D. J. Computer simulation of final-stage sintering: I, Model, kinetics, and microstructure. *J. Am. Ceram. Soc.* **73**, 2857-2864 (1990).
50. Chen, I. W., Hassold, G. N., Srolovitz, D. J. Computer simulation of final-stage

- sintering: II, Influence of initial pore size. *J. Am. Ceram. Soc.* **73**, 2865-2872 (1990).
51. Chen, I. W., Wang, X. H. Sintering dense nanocrystalline ceramics without final-stage grain growth. *Nature* **404**, 168-171 (2000).
52. Wang, X. H., Chen, P. L., Chen, I. W. Two-step sintering of ceramics with constant grain-size, I. Y_2O_3 . *J. Am. Ceram. Soc.* **89**, 431-437 (2006).
53. Lee, Y. I., Kim, Y. W., Mitomo, M., Kim, D. Y. Fabrication of dense nanostructured silicon carbide ceramics through two-step sintering. *J. Am. Ceram. Soc.* **86**, 1803-1805 (2003).
54. Jiang, H., Wang, X., Lei, W., Fan, G., Lu, W. Effects of two-step sintering on thermal and mechanical properties of aluminum nitride ceramics by impedance spectroscopy analysis. *J. Eur. Ceram. Soc.* **39**, 249-254 (2019).
55. Yang, H., Li, L., Cao, W., Liu, Y., Mukhtar, M., Zhao, L., Kang, Y., Dong, Y., Li, J. Sintering kinetics and microstructure evolution in $\alpha\text{-Al}_2\text{O}_3$ nanocrystalline ceramics: Insensitive to Fe impurity. *J. Eur. Ceram. Soc.* **40**, 1505-1512 (2020).
56. Li, L., Pu, S., Liu, Y., Zhao, L., Ma, J., Li, J. High-purity disperse $\alpha\text{-Al}_2\text{O}_3$ nanoparticles synthesized by high-energy ball milling. *Adv. Powder Tech.* **29**, 2194-2203 (2018).

Acknowledgement

I.W.C. and Y.D. acknowledge the support by the Department of Energy (BES grant no. DEFG02-11ER46814) and the LRSM facilities funded by the U.S. National Science Foundation (grant no. DMR-1120901) during Y.D.'s PhD research at the University of

Pennsylvania that initiated the present work. Ju L. and Y.D. acknowledge the support by NSF CMMI-1922206. Ju L., Y.D. and D.D. acknowledge support by the U.S. Department of Energy (USDOE), Office of Energy Efficiency and Renewable Energy (EERE), Advanced Manufacturing Office (AMO) R&D Projects Emerging Research Exploration, under DOE Idaho Operations Office with contract no. DE-AC07-05ID14517. Jiangong L. and H.Y. acknowledge the support by the National Natural Science Foundation of China (51772137) and the Fundamental Research Funds for the Central Universities (lzujbky-2019-sp03).

Author contributions

Y.D., Ju L., Jiangong L. and I.W.C. conceived the project. Y.D. and H.Y. conducted the research. All authors discussed and contributed to writing.

Competing financial interests

The authors declare no competing financial interests.

Supplementary Information

Ultra-uniform Nanocrystalline Materials via Two-Step Sintering

Yanhao Dong¹, Hongbing Yang², Dong Ding³, Ju Li^{1,4,*}, Jian-Gong Li^{2,*},

I-Wei Chen^{5,*}

*¹Department of Nuclear Science and Engineering, Massachusetts Institute of
Technology, Cambridge, MA 02139, USA*

*²Institute of Materials Science and Engineering and MOE Key Laboratory for Special
Functional Materials and Structure Design, Lanzhou University, Lanzhou 730000,
China*

*³Energy & Environmental Science and Technology, Idaho National Laboratory,
Idaho Falls, ID 83415, USA*

*⁴Department of Materials Science and Engineering, Massachusetts Institute of
Technology, Cambridge, MA 02139, USA*

*⁵Department of Materials Science and Engineering, University of Pennsylvania,
Philadelphia, PA 19104, USA*

Table of content

Supplementary Figures S1-S4	Page 2
Supplementary Table S1	Page 6

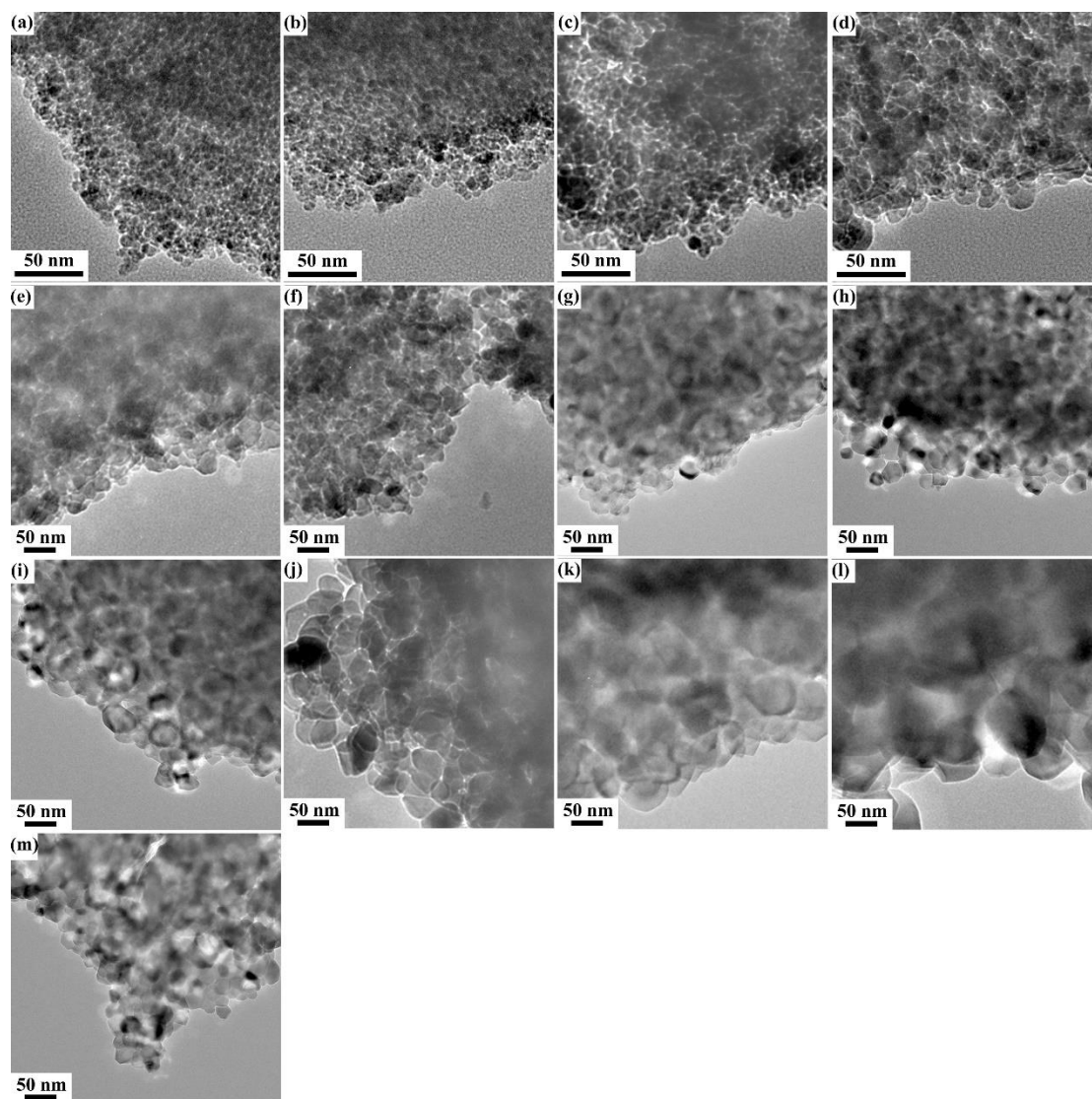


Figure S1 TEM images of Al_2O_3 heated to (a) 700°C, (b) 800°C, (c) 900°C, (d) 1000°C, (e) 1050°C, (f) 1100°C, (g) 1125°C, (h) 1150°C, (i) 1175°C, (j) 1200°C, (k) 1250°C, and (l) 1300°C, all without holding. (m) Two-step sintered Al_2O_3 at 1150°C (T_1) without holding and then at 1025°C (T_2) for 40 h.

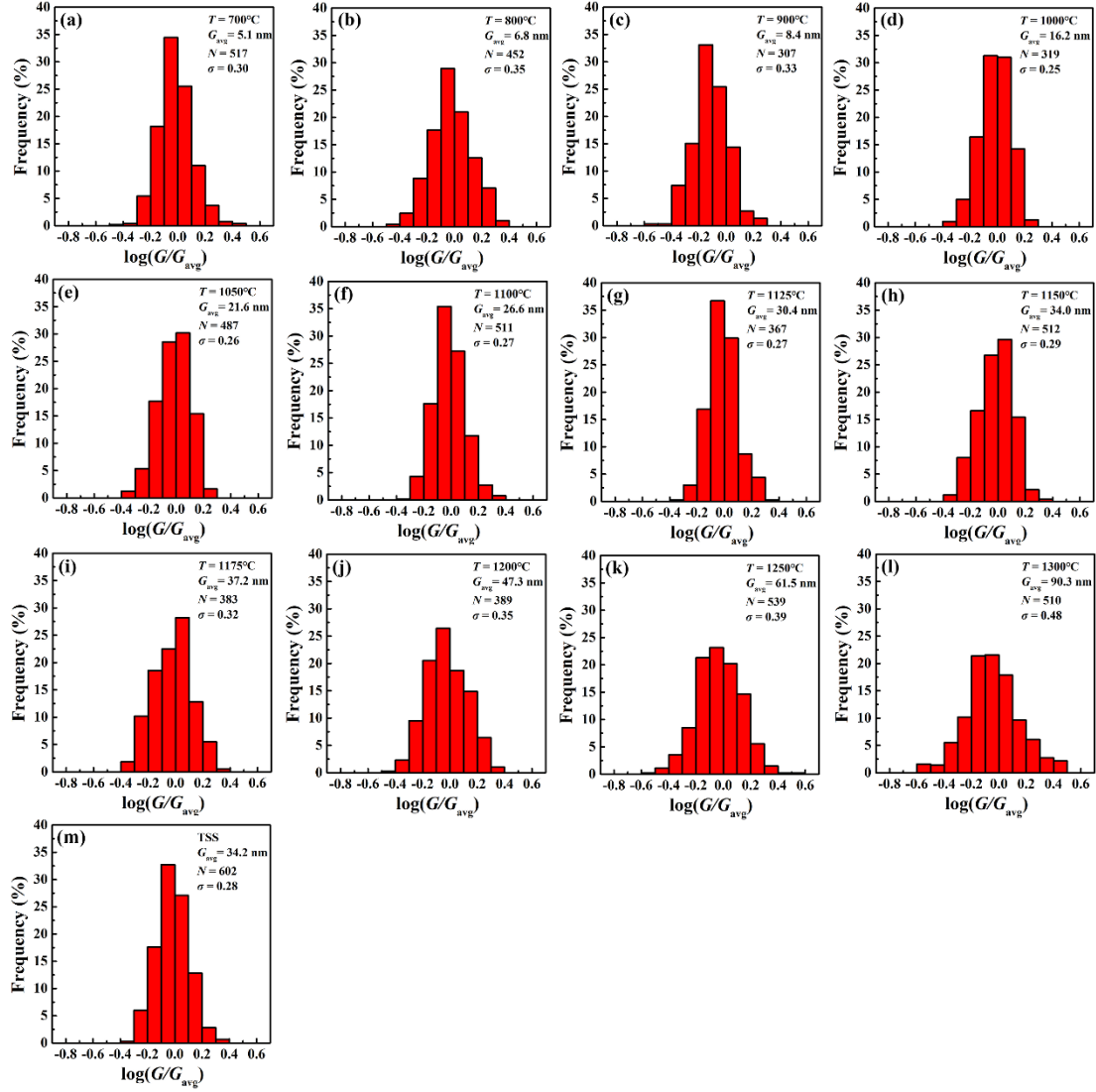


Figure S2 Normalized grain size distribution measured from TEM images in **Fig. S1**.

Also listed are G_{avg} , number N of measured grains and σ . Al_2O_3 samples were sintered at (a) 700°C, (b) 800°C, (c) 900°C, (d) 1000°C, (e) 1050°C, (f) 1100°C, (g) 1125°C, (h) 1150°C, (i) 1175°C, (j) 1200°C, (k) 1250°C, and (l) 1300°C, all without holding. (m) Two-step sintered Al_2O_3 at 1150°C (T_1) without holding and then at 1025°C (T_2) for 40 h.

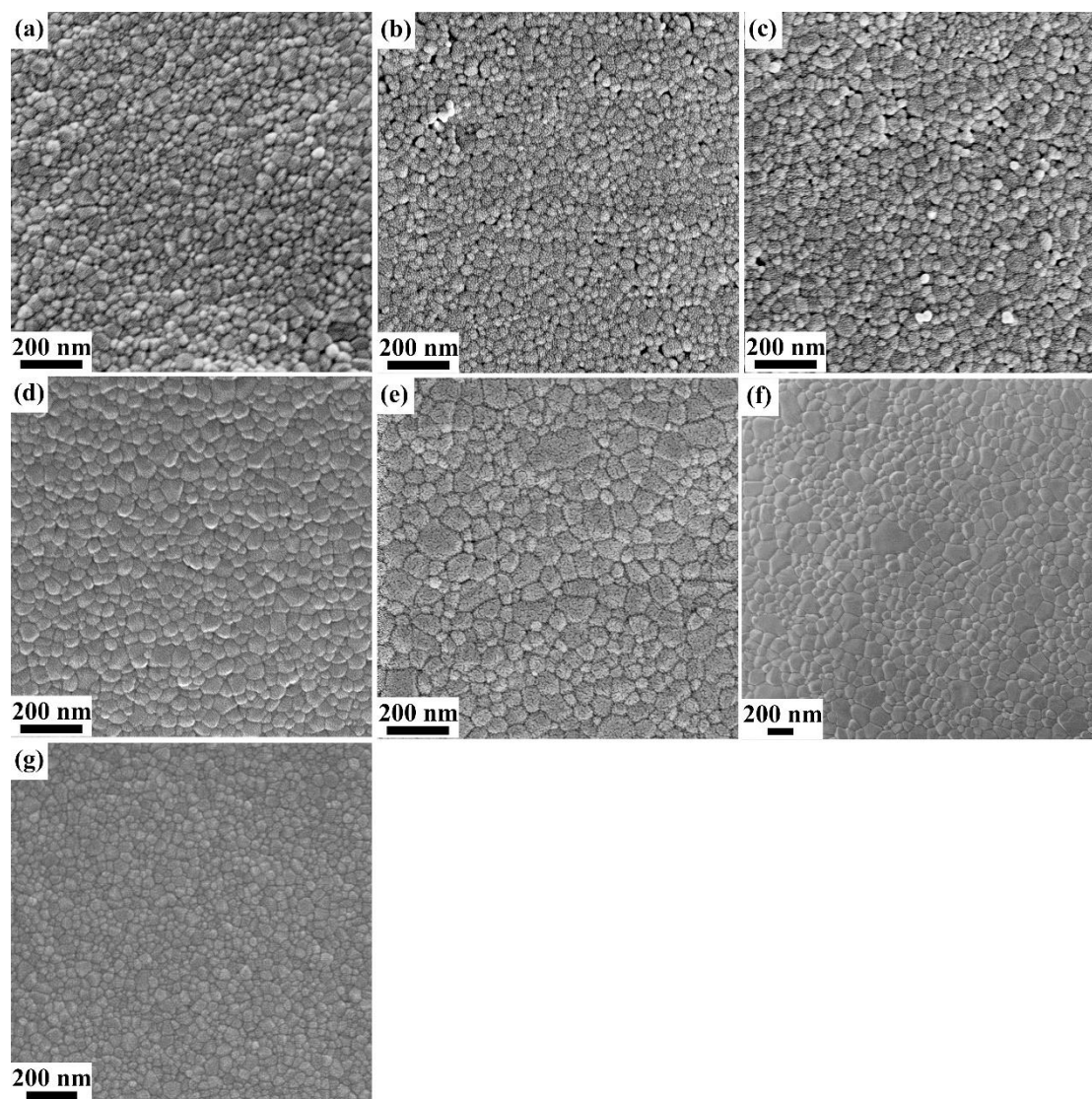


Figure S3 SEM images of Al_2O_3 sintered at (a) 1125°C, (b) 1150°C, (c) 1175°C, (d) 1200°C, (e) 1250°C, and (f) 1300°C, all without holding. (g) Two-step sintered Al_2O_3 at 1150°C (T_1) without holding and then at 1025°C (T_2) for 40 h.

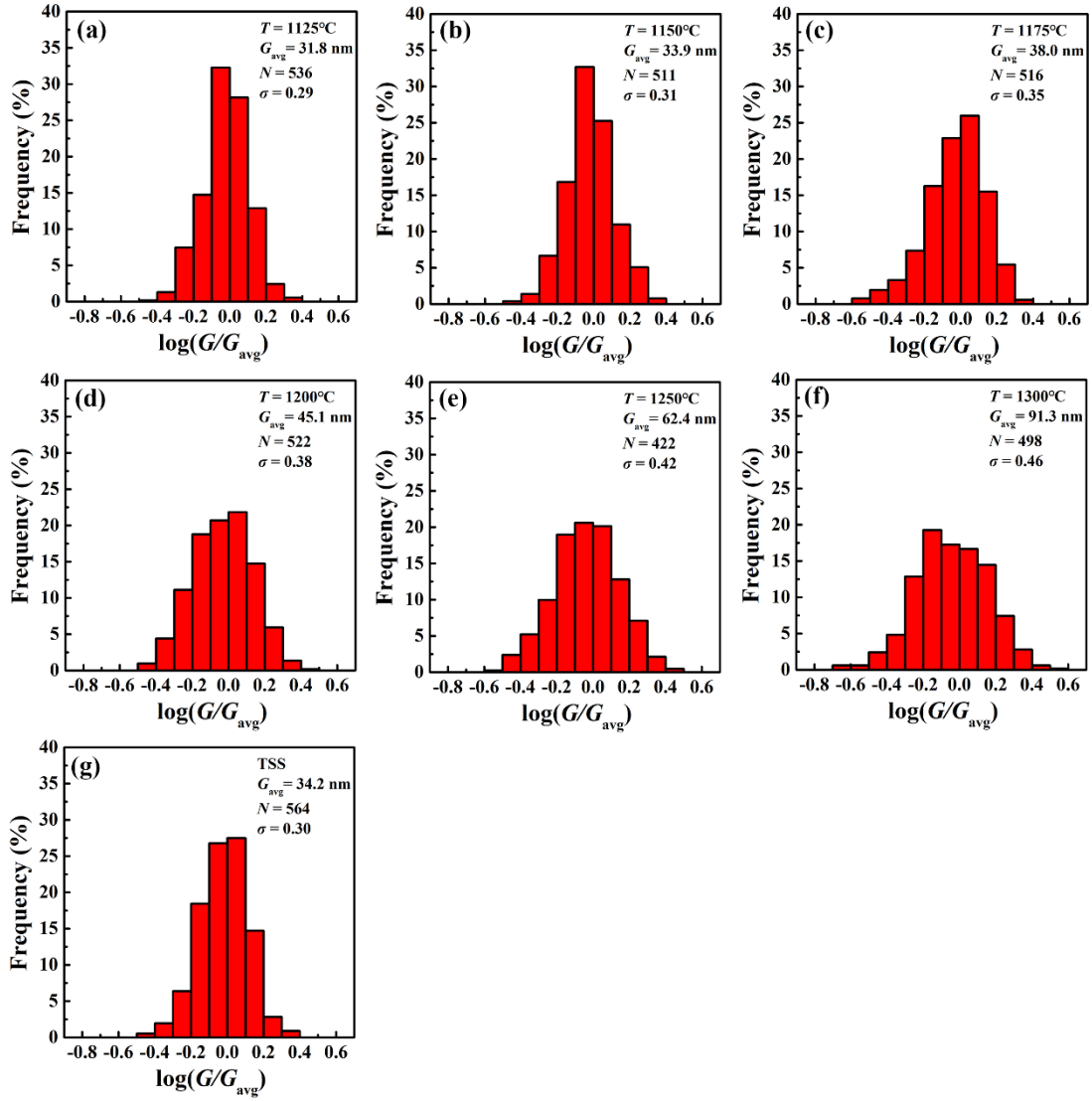


Figure S4 Normalized grain size distribution measured from SEM images in **Fig. S3**.

Also listed are G_{avg} , number N of measured grains and σ . Al_2O_3 samples were sintered at (a) 1125°C, (b) 1150°C, (c) 1175°C, (d) 1200°C, (e) 1250°C, and (f) 1300°C, all without holding. (g) Two-step sintered Al_2O_3 at 1150°C (T_1) without holding and then at 1025°C (T_2) for 40 h.

Table S1 Measured G_{avg} , N and σ for dense polycrystalline materials. Materials processed by two-step sintering in red, and by other techniques in blue.

Materials	Symbol	G_{avg}	N	σ	Reference
Al_2O_3	Filled square	385nm	431	0.57	This work
Al_2O_3	Filled square	0.33 μm	209	0.50	Fig. 2a, Ref. 10
Al_2O_3	Filled square	4.0 μm	261	0.69	Fig. 3a, Ref. 11
Al_2O_3	Filled square	4.4 μm	421	0.39	Fig.1a, Ref. 12
Al_2O_3	Filled square	31.4 μm	510	0.65	Fig.1d, Ref. 12
Al_2O_3	Filled square	0.24 μm	148	0.46	Fig.3, Ref. 13
Al_2O_3	Filled square	1.1 μm	216	0.48	Fig.8b, Ref. 14
Al_2O_3	Filled square	34nm	564	0.30	This work
Al_2O_3	Filled square	55nm	525	0.34	Fig. 6, Ref. 15
Al_2O_3	Filled square	41nm	536	0.36	Fig. 7a, Ref. 16
Al_2O_3	Filled square	32nm	612	0.34	Fig. 7b, Ref. 16
Al_2O_3	Filled square	54nm	530	0.34	Fig. 7c, Ref. 16
BaTiO_3	Open square	0.16 μm	129	0.48	Fig. 2b, Ref. 8
BaTiO_3	Open square	1.2 μm	223	0.37	Fig. 4f, Ref. 17
BaTiO_3	Open square	0.15 μm	145	0.46	Fig. 2c, Ref. 8
BaTiO_3	Open square	0.16 μm	127	0.44	Fig. 2d, Ref. 8
BaTiO_3	Open square	68nm	532	0.37	Fig. 4b, Ref. 17
BaTiO_3	Open square	98nm	357	0.42	Fig. 4c, Ref. 17
BaTiO_3	Open square	0.20 μm	521	0.38	Fig. 4d, Ref. 17
$\text{BaZr}_{0.1}\text{Ce}_{0.7}\text{Y}_{0.1}\text{Yb}_{0.1}\text{O}_{3-x}$	Half-filled square	0.49 μm	98	0.40	Fig.3a, Ref. 18
$\text{BaZr}_{0.1}\text{Ce}_{0.7}\text{Y}_{0.1}\text{Yb}_{0.1}\text{O}_{3-x}$	Half-filled square	0.57 μm	80	0.40	Fig.3b, Ref. 18
$\text{BaZr}_{0.1}\text{Ce}_{0.7}\text{Y}_{0.1}\text{Yb}_{0.1}\text{O}_{3-x}$	Half-filled square	0.30 μm	229	0.36	Fig.3c, Ref. 18
$\text{BaZr}_{0.1}\text{Ce}_{0.7}\text{Y}_{0.1}\text{Yb}_{0.1}\text{O}_{3-x}$	Half-filled square	1.3 μm	486	0.36	Fig.5a, Ref. 19
$\text{BaZr}_{0.1}\text{Ce}_{0.7}\text{Y}_{0.1}\text{Yb}_{0.1}\text{O}_{3-x}$	Half-filled square	2.3 μm	176	0.39	Fig.5b, Ref. 19
CeO_2	Filled cycle	0.67 μm	115	0.49	Fig. 2a, Ref. 20

CeO ₂	Filled cycle	0.39μm	119	0.44	Fig. 2b, Ref. 20
CeO ₂	Filled cycle	16.6μm	93	0.52	Fig. 2c, Ref. 20
CeO ₂	Filled cycle	0.54μm	76	0.42	Fig. 2d, Ref. 20
CeO ₂	Filled cycle	20.9μm	74	0.43	Fig. 2e, Ref. 20
Gd _{0.1} Ce _{0.9} O _{1.95}	Open cycle	0.51μm	237	0.43	Fig.1c, Ref. 21
Gd _{0.1} Ce _{0.9} O _{1.95}	Open cycle	0.77μm	231	0.38	Fig.5b, Ref. 22
(K,Na,Li)(Nb,Ta,Sb)O ₃	Half-filled cycle	1.6μm	190	0.60	Fig.5d, Ref. 23
Li ₇ La ₃ Zr ₂ O ₁₂	Filled triangle	5.4μm	426	0.49	Fig.1b, Ref. 24
Li ₇ La ₃ Zr ₂ O ₁₂	Filled triangle	2.2μm	332	0.41	Fig.3a, Ref. 25
Li ₇ La ₃ Zr ₂ O ₁₂	Filled triangle	29.1μm	233	0.47	Fig.3b, Ref. 25
Li ₇ La ₃ Zr ₂ O ₁₂	Filled triangle	39.2μm	144	0.46	Fig.3c, Ref. 25
Li ₇ La ₃ Zr ₂ O ₁₂	Filled triangle	37.6μm	150	0.47	Fig.3d, Ref. 25
(La,Sr)(Ga,Mg)O ₃	Open triangle	1.8μm	121	0.46	Fig.1c, Ref. 26
(La,Sr)(Ga,Mg)O ₃	Open triangle	2.2μm	131	0.42	Fig.1d, Ref. 26
(La,Sr)(Ga,Mg)O ₃	Open triangle	2.0μm	161	0.36	Fig.2a, Ref. 27
(La,Sr)(Ga,Mg)O ₃	Open triangle	3.4μm	260	0.39	Fig.6c, Ref. 28
(La,Sr)(Ga,Mg)O ₃	Open triangle	5.0μm	139	0.37	Fig.6d, Ref. 28
Lu ₃ Al ₅ O ₁₂	Half-filled triangle	0.39μm	218	0.38	Fig.3a, Ref. 29
MgO	Filled diamond	72nm	212	0.43	Fig.1a, Ref. 30
MgAl ₂ O ₄	Open diamond	93nm	145	0.40	Fig.3c, Ref. 31
MgAl ₂ O ₄	Open diamond	85nm	171	0.45	Fig.3d, Ref. 31
NaNbO ₃	Half-filled diamond	4.8μm	156	0.36	Fig.4a, Ref. 32
(Pb,La)(Zr,Ti)O ₃	Filled hexagon	3.2μm	532	0.48	Fig. 16, Ref. 33
(Pb,La)(Zr,Ti)O ₃	Filled hexagon	1.2μm	111	0.44	Fig.18, Ref. 34
SrTiO ₃	Open hexagon	5.8μm	421	0.68	Fig. 3a, Ref. 35
SrTiO ₃	Open hexagon	4.3μm	457	0.96	Fig. 3b, Ref. 35
SrTiO ₃	Open hexagon	3.3μm	445	0.81	Fig. 3c, Ref. 35
SrTiO ₃	Open hexagon	14.0μm	506	0.60	Fig. 3d, Ref. 35
SrTiO ₃	Open hexagon	2.6μm	462	0.78	Fig. 5a, Ref. 35

SrTiO ₃	Open hexagon	3.6μm	422	0.84	Fig. 5b, Ref. 35
SrTiO ₃	Open hexagon	5.1μm	470	0.98	Fig. 5c, Ref. 35
SrTiO ₃	Open hexagon	2.2μm	519	0.69	Fig. 7a, Ref. 35
SrTiO ₃	Open hexagon	3.1μm	545	0.75	Fig. 7b, Ref. 35
SrTiO ₃	Open hexagon	3.8μm	440	0.86	Fig. 7c, Ref. 35
TiO ₂	Half-filled hexagon	0.13μm	371	0.40	Fig. 6, Ref. 36
W	Filled pentagon	1.8μm	371	0.54	Fig. 5a, Ref. 37
W	Filled pentagon	0.83μm	549	0.41	Fig. 5b, Ref. 37
Y ₂ O ₃	Open pentagon	4.1μm	54	0.42	Fig. 3b, Ref. 38
Y ₂ O ₃	Open pentagon	0.73μm	85	0.40	Fig. 3c, Ref. 38
Y ₂ O ₃	Open pentagon	0.23μm	98	0.42	Fig. 3d, Ref. 38
Y ₂ O ₃	Open pentagon	0.31μm	70	0.45	Fig. 3e, Ref. 38
Y ₃ Al ₅ O ₁₂	Half-filled pentagon	0.42μm	71	0.46	Fig. 8a, Ref. 39
Y ₃ Al ₅ O ₁₂	Half-filled pentagon	24.5μm	431	0.44	Fig. 1, Ref. 40
Y ₃ Fe ₅ O ₁₂	Open star	5.1μm	235	0.38	Fig. 5a, Ref. 41
ZnO	Half-filled star	0.34μm	469	0.37	Fig. 7b, Ref. 42
3 mol% Y ₂ O ₃ -ZrO ₂	Plus	78nm	521	0.32	Fig. 6a, Ref. 43
3 mol% Y ₂ O ₃ -ZrO ₂	Plus	0.21μm	130	0.39	Fig. 6b, Ref. 43
3 mol% Y ₂ O ₃ -ZrO ₂	Plus	88nm	469	0.43	Fig. 6c, Ref. 43
8 mol% Y ₂ O ₃ -ZrO ₂	Cross	1.19μm	354	0.53	This work
8 mol% Y ₂ O ₃ -ZrO ₂	Cross	0.27μm	427	0.34	Fig. 9b, Ref. 44
8 mol% Y ₂ O ₃ -ZrO ₂	Cross	0.34μm	523	0.41	Fig. 2c, Ref. 45